

See discussions, stats, and author profiles for this publication at: <https://www.researchgate.net/publication/26702023>

Electronic structure of the tyrosine D radical and the water-splitting complex from pulsed ENDOR spectroscopy on photosystem II single crystals

ARTICLE *in* PHYSICAL CHEMISTRY CHEMICAL PHYSICS · SEPTEMBER 2009

Impact Factor: 4.49 · DOI: 10.1039/b908093g · Source: PubMed

CITATIONS

32

READS

31

6 AUTHORS, INCLUDING:



Christian Teutloff

Freie Universität Berlin

48 PUBLICATIONS 853 CITATIONS

SEE PROFILE



Matthias Broser

Humboldt-Universität zu Berlin

15 PUBLICATIONS 952 CITATIONS

SEE PROFILE



Athina Zouni

Humboldt-Universität zu Berlin

92 PUBLICATIONS 6,665 CITATIONS

SEE PROFILE

Electronic structure of the tyrosine D radical and the water-splitting complex from pulsed ENDOR spectroscopy on photosystem II single crystals†

Christian Teutloff,^a Susanne Pudollek,^a Sven Keßen,^a Matthias Broser,^b Athina Zouni^b and Robert Bittl^{*a}

Received 22nd April 2009, Accepted 30th June 2009

First published as an Advance Article on the web 14th July 2009

DOI: 10.1039/b908093g

Pulsed electron nuclear double resonance (ENDOR) spectroscopy at Q- and W-band frequencies was applied to single crystals of photosystem II from *Th. elongatus*. W-Band ¹H-ENDOR on the dark-stable radical state Y_D[•] of the redox-active tyrosine residue Y_D yields a complete mapping of the electronic structure of this amino acid radical in terms of an assignment of all hyperfine coupling tensors of the protons covalently bound to the side chain. This study can serve as a model case for the potential of high-field/high-frequency ENDOR on protein single crystals for obtaining highly resolved electronic structure information. Q-band ⁵⁵Mn-ENDOR was applied to the S₂ oxidation state of the water-splitting complex in photosystem II single crystals. Irrespective of the difficulties arising from the extremely broad electron paramagnetic resonance (EPR) spectroscopy (≈200 mT) and ENDOR (≈100 MHz) spectra a tentative assignment of the Mn ion in the formal oxidation state III to a Mn position in the structural model of PSII is possible on the basis of the ENDOR data.

Introduction

The two large membrane-bound pigment–protein complexes photosystem I (PSI) and photosystem II (PSII) are the sites of the light reactions in oxygenic photosynthesis. PSI is a light-driven plastocyanin:ferredoxin oxidoreductase transferring electrons from plastocyanin on the lumenal side to ferredoxin on the stromal side of the thylakoid membrane, in essence working as a molecular solar cell.¹ PSII is a light-driven water:plastoquinone oxidoreductase transferring electrons from water on the lumenal side to an exchangeable plastoquinone cofactor at the stromal side.² Molecular oxygen is formed as a by-product of the light-driven water oxidation in PSII. The catalytic site for the water splitting and oxygen evolution, the water-oxidising complex (WOC), is a manganese–calcium complex consisting of four manganese ions and a calcium ion connected *via* several μ-oxo bridges (Mn₄O_x–Ca complex).^{3,4} The WOC is coupled to the chlorophyll moieties making up the site of initial electron transfer after photo-excitation by a redox-active tyrosine amino acid residue (Y_Z).^{5,6} The cofactors of the electron transfer chain in PSII are embedded in the hetero-dimeric reaction centre core of two

protein subunits, D1 and D2. These two subunits show a high sequence homology and are arranged in a pseudo-C₂ symmetry leading to two almost symmetric branches of electron transfer cofactors except the WOC. Symmetrically to Y_Z, a second redox-active tyrosine residue, Y_D, is found. This residue is also coupled to the electron transfer chain and forms under light illumination a dark-stable radical, Y_D[•]. The functional role of Y_D is so far not understood in detail and mutants lacking Y_D are able to maintain photo-autotrophic growth.⁷

Electron paramagnetic resonance (EPR) spectroscopy has proven to be a valuable tool in the study of photosynthesis as the light-induced single-electron transfer leads to a sequence of paramagnetic intermediates of the organic electron transfer cofactors⁸ as well as the WOC.⁹ The four-electron reaction of water oxidation requires the accumulation of four oxidising equivalents in the WOC. In the model for water oxidation put forward by Kok *et al.*,¹⁰ the WOC passes through four (meta)stable oxidation states S_{0–3} and a transition state S₄. The dark-stable ground state is the S₁-state. The S₂-state generated after one photon absorption is paramagnetic and has extensively been studied by EPR techniques.^{11–16} The initial observation of a multi-line signal (MLS) in EPR spectroscopy by Dismukes and Siderer¹⁷ was the first evidence for the involvement of a mixed-valent manganese cluster in the WOC.

Even after the availability of structural models for PSII from X-ray crystallography^{18–23} information on the geometric and electronic structure of the WOC from spectroscopy remains essential. Owing to radiation damage²⁴ the current X-ray structures of the WOC probably do not correspond to any of the functional S-state structures. Furthermore, neither the bridging μ-oxo nor the amino acid ligands have been assigned unambiguously by X-ray crystallography so far. An

^a Fachbereich Physik, Freie Universität Berlin, Berlin, Germany.
E-mail: robert.bittl@fu-berlin.de

^b Max-Volmer-Laboratorium, Technische Universität Berlin, Berlin, Germany

† Electronic supplementary information (ESI) available: Orientational information of the single crystals used for Y_D[•] ¹H-ENDOR at W-band and WOC S₂-state ⁵⁵Mn-ENDOR at Q-band in the laboratory frames, complete 94 GHz single crystal Y_D[•] ENDOR data sets (including simulations of the individual spectra), and Q-band Y_D[•] EPR for the single crystal used for the WOC S₂-state ⁵⁵Mn-ENDOR are given. See DOI: 10.1039/b908093g

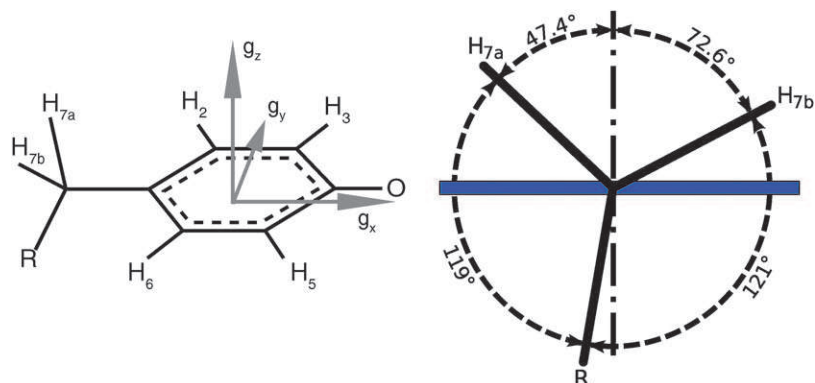


Fig. 1 Left: The tyrosine with its molecular coordinate system. The g -tensor axes are collinear to the molecular axes. Right: Newman projection along the C7–C4 axis of Y_D^\bullet showing the inclined position of the two β -protons with respect to the (dash-dotted) plane normal.

important challenge for spectroscopic investigations of the structure of the WOC is an assignment of redox states to the individual Mn ions. This knowledge is a prerequisite for validating models for the catalytic reaction mechanism of water splitting and oxygen evolution at the WOC.

The purpose of the present study is two-fold. First, we present a continuation of the characterisation of the dark-stable Y_D^\bullet by high-field/high-frequency (94 GHz, W-band) EPR spectroscopy on PSII single crystals²⁵ by extending the approach to W-band electron nuclear double resonance (ENDOR) spectroscopy in PSII crystals. The goal of this study is a complete assignment of all hyperfine couplings (hfc) of the protons bound to the tyrosine side chain to specific atom positions. Previous EPR and ENDOR studies have shown that the magnetic equivalency of the protons at positions 3/5 and 2/6, respectively (see Fig. 1), of an isolated tyrosine residue are lifted for Y_D^\bullet in PSII^{25,26} due to the asymmetric protein environment. This approach serves as a model study to show the potential of high-field/high-frequency EPR/ENDOR on protein single crystals for obtaining highly resolved electronic structure information.

The second part of this study deals with the first ^{55}Mn -ENDOR spectra from the S_2 -state of the WOC in PSII single crystals. Up to now few studies have been published on ^{55}Mn -ENDOR spectroscopy from the S_2 -state of the WOC in frozen-solution PSII samples.^{27–30} The large width of the S_2 -state MLS of about 200 mT and the large spectral width of the corresponding ^{55}Mn -ENDOR spectra of about 100 MHz render the acquisition of these ENDOR spectra already a difficult task in frozen-solution samples, and all spectra published so far have only a moderate signal-to-noise ratio (S/N). The difficulty in recording ^{55}Mn -ENDOR spectra of the S_2 -state in PSII single crystals is increased significantly by the fact that the obtainable crystal size is rather small. The S_2 -state ^{55}Mn -ENDOR spectra presented here nevertheless allow already a qualitative assignment of the orientation of the Mn ion in the WOC carrying the largest hyperfine coupling.

Materials and methods

Preparation and crystallisation of PSII core complexes (PSIIcc) from *Th. elongatus* are described elsewhere.³¹ For Q-band measurements a single crystal was put into a quartz

tube [1 mm inner diameter (i.d.), 2.9 mm outer diameter (o.d.)] and frozen in liquid nitrogen. It was illuminated about 2 min at 200 K with a 180 W halogen lamp immediately before the EPR experiments. The sample tube was transferred into the cryostat, which was pre-cooled to 80 K, after illumination.

The Q-band measurements were performed on a Bruker BioSpin Elexsys E580 spectrometer equipped with a Super QFT upgrade, an Amplifier Research 250A250S RF-Amplifier and a home-built Q-band ENDOR resonator. All EPR and ENDOR spectra were recorded at a sample temperature $T = 5$ K and at a microwave frequency $\nu = 33.85$ GHz. The field-swept echo (FSE) spectra were acquired using a two-pulse sequence ($\pi/2 - \tau - \pi - \tau$ -echo) with microwave (mw) pulse lengths of 32 ns and 64 ns for the $\pi/2$ - and π -pulses, respectively. For the Davies-ENDOR sequence ($\pi - T - \pi/2 - \tau - \pi - \tau$ -echo) the same pulse lengths were used, the radio frequency (RF) pulse during the time interval T had a length of 4 μs . The shot repetition time was 800 μs . All ENDOR spectra were recorded in stochastic mode.

For the W-band experiments a PSII solution in 100 mM PIPES buffer at pH 7.0, including 5 mM CaCl_2 and 0.03% β -DM with a chlorophyll concentration of 13 mM were filled into quartz tubes (0.7 mm i.d., 0.87 mm o.d.) and frozen in liquid nitrogen. Single crystals of PSIIcc soaked in 100 mM PIPES buffer at pH 7.0, including 5 mM CaCl_2 , 10% w/w PEG 2000 and 25% w/w glycerol, were sucked with a drop of mother liquor into W-band quartz capillaries and rapidly frozen in liquid nitrogen in an arbitrary orientation.

W-Band spectra were recorded on a Bruker Biospin Elexsys E680 spectrometer including an E680-PU power upgrade, a Bruker Teraflex EN600-1021H ENDOR resonator and a Amplifier Research 140A400 RF-amplifier. All spectra were acquired at 40 K. For FSE spectra a typical Hahn-echo sequence, for ENDOR the Davies-type sequence (see above) was utilised. Pulse lengths and shot repetition times are given in the respective figure captions.

Analysis. Simulation and fitting of the pseudo-modulated Y_D^\bullet W-band EPR spectra were achieved by a self-written MATLAB macro based on first-order perturbation theory for the resonance position and utilising a random-walk procedure from random starting points, checking at each step for the lowest χ^2 deviation from the measured spectra. Other home-written MATLAB macros using first-order perturbation theory

were employed to simulate the ENDOR spectra recorded on frozen solution and single crystals. No automatic fitting algorithm was applied to the ENDOR spectra due to the inherent difficulties with signal intensity and linewidths and unresolved underlying signals at RF frequencies close to the free proton Larmor frequency. Parameters were changed manually to achieve the best possible simultaneous simulation of all available ENDOR measurements—orientation-selective frozen-solution spectra and rotation patterns of the crystal spectra—with one consistent parameter set.

The simulation of the high-frequency part of the ^{55}Mn ENDOR spectrum of frozen-solution *Th. elongatus* samples was done with *EasySpin*,³² a MATLAB toolbox, based on a matrix-diagonalisation algorithm. Calculation of the high-frequency ^{55}Mn -ENDOR transitions of the crystal spectra was based on a second-order perturbation theory approach.³³

Results & discussion

High-field EPR and ENDOR on $\text{Y}_\text{D}^\bullet$

Single-crystal EPR at 94 GHz. The scope of this part of our work was a complete characterisation of the hf structure of the $\text{Y}_\text{D}^\bullet$ tyrosine radical in PSII. Using the advantages of single-crystal EPR and ENDOR spectroscopy we set out to differentiate between the proton couplings at the 3/5 and 2/6 positions, respectively (see Fig. 1). These protons are magnetically equivalent in symmetric environments but are slightly inequivalent due to the protein environment of $\text{Y}_\text{D}^\bullet$ in PSII, e.g. due to a hydrogen bond to His189 in subunit PsbD. The starting point for achieving this goal were orientation-dependent EPR spectra recorded for $\text{Y}_\text{D}^\bullet$ in a PSII single crystal shown in Fig. 2. These spectra were recorded in FSE mode but are shown here after pseudo-modulation in the cw-EPR typical derivative mode. The derivative mode allows a better visual judgement of the simulation quality as it shows significantly more spectral structures than the integrated spectra. Upon rotation around an axis close to the long morphological axis of the PSII crystal, every 10° a spectrum was recorded. Due to the $P2_12_12_1$ symmetry of the unit cell and the dimeric character of *Th. elongatus* PSII in the crystal, 8 inequivalent $\text{Y}_\text{D}^\bullet$ contribute to the EPR spectrum. The resulting rotation pattern was first simulated by using the values for the principal values of the g -tensor, the principal values of the three large hfc (H3, H5, H7a) and their orientation within the $\text{Y}_\text{D}^\bullet$ moiety reported by Hofbauer *et al.*²⁵ As fitting parameters we used the orientation of the g -axes within the crystallographic coordinate system together with the orientation of the crystal within the laboratory frame. With this approach we readily achieved a good fit of the EPR spectra (data not shown). The obtained orientation of the crystal rotation axis was found to be in the vicinity of the crystallographic b -axis and its orientation within the crystallographic coordinate system is given in Table S1 in the ESI.† The rather small deviation of the rotation axis from the crystallographic b -axis results in pairs of closely varying lines in Fig. 2 indicating the g -factors of the 8 inequivalent $\text{Y}_\text{D}^\bullet$ sites in the unit cell. A perfect alignment of the crystal rotation axis with one of the crystallographic axes in a $P2_12_12_1$ symmetry

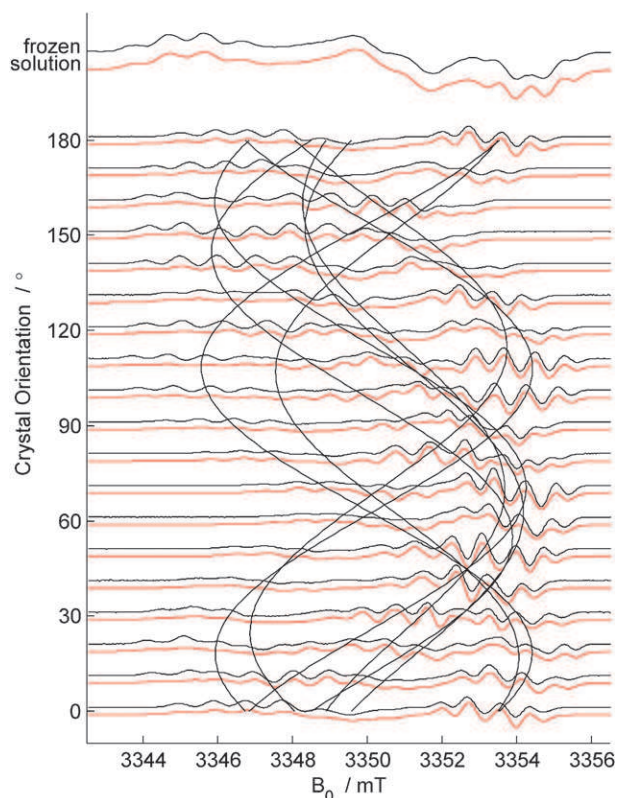


Fig. 2 Orientation-dependent EPR at 94 GHz of $\text{Y}_\text{D}^\bullet$ from *Th. elongatus* together with simulation (red). The orientation dependence of the particular magnetic inequivalent crystal sites are indicated. Top: frozen-solution spectrum. The spectra were acquired at 40 K with a shot repetition time of 2 ms, the π -pulse length was 128 ns.

group would result in a pairwise magnetic degeneracy of the four PSII dimers and thus to four instead of eight inequivalent $\text{Y}_\text{D}^\bullet$ sites.

The simulations indicate that between 60° and 70° the crystallographic a -axis is almost parallel to the magnetic field. This leads to the rather complete degeneracy of all four PSII monomers connected by the crystal symmetry and the only remaining splitting into one set at a g -factor corresponding to about 3350 mT and a second set at about 3353 mT is due to the non-crystallographic PSII dimer symmetry.

The resulting g -tensor orientation within the crystallographic coordinate system corroborated the result reported by Hofbauer.²⁵ As the focus of this study was not an improvement of the EPR-derived orientation of $\text{Y}_\text{D}^\bullet$ in the protein structure, but a full characterisation of the $\text{Y}_\text{D}^\bullet$ hyperfine structure, we already state here a summary regarding the $\text{Y}_\text{D}^\bullet$ orientation. Even with our final set of hfc parameters, in the best simulations of the EPR spectra, as shown in Fig. 2, the $\text{Y}_\text{D}^\bullet$ orientation in the protein structure remains virtually unchanged compared to the result from Hofbauer *et al.*²⁵

It is particularly interesting to note that this EPR-derived structure deviated until recently from the structure derived from X-ray crystallography as shown in Fig. 3, comparing our orientation with that from PDB entry 2AXT of PSII at 3.0 Å resolution.²² However, in the most recent X-ray structure at 2.9 Å resolution²³ (PDB entries 3BZ1/3BZ2) the Y_D

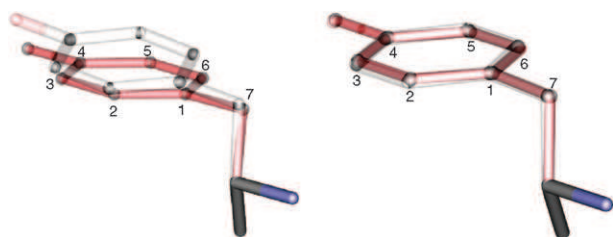


Fig. 3 Comparison between the Y_D orientations from the crystal structure (transparent) and from the orientation determined for Y_D^\bullet by W-band EPR (red) on single crystals. Left: Structure from Loll *et al.*²² (PDB entry 2AXT). Right: Comparison with the structure from Guskov *et al.*²³ (PDB entry 3BZ1).

orientation converged towards the EPR-derived orientation, also shown in Fig. 3 and Table 1.

Orientation-selective ^1H -ENDOR on frozen solution at 94 GHz. As additional independent hfc data turned out to be essential for the initial simulation of Y_D^\bullet single-crystal ENDOR spectra we augmented the available hfc data by orientation-selective ENDOR spectroscopy on frozen solution. The merit of this approach for obtaining hf principal values and the orientation of hfc tensors with respect to g -tensor axes was shown, *e.g.* by Rohrer *et al.*³⁴ and Bennati *et al.*³⁵ A set of seven orientation-selective ENDOR spectra is depicted in Fig. 4. They were acquired at the field positions marked within the frozen-solution EPR spectrum shown in the inset, starting with the spectrum at the low field edge (g_x , bottom) of the tyrosine EPR signal and ending at the high-field edge (g_z , top). In order to facilitate the comparison between the spectra taken at different magnetic field values and thus different free proton Larmor frequencies ν_L , all RF frequencies ν_{rf} are normalised to the appropriate ν_L . The spectra are displayed as $|\nu_{rf} - \nu_L|$ spectra after symmetrisation of the low- and high-frequency halves of the spectra.

The starting point for the analysis of these complex spectra are previous high-field EPR and X-band ENDOR studies^{25,26,36–38} and theory,³⁹ which show the outmost peaks to belong to one of the β -protons at position H7a/b and the broad signals around 14 (g_x), 5 (g_y) and 10 MHz (g_z) to belong to the protons in the H3 and H5 positions. Most of the principal values of the hyperfine tensors are well resolved, *e.g.* H3's and H5's A_x component appear clearly separated from the β -proton H7a and each other (see the two resonances around 13 MHz in the spectrum recorded at 3345 mT), unlike in X-band studies. A_y on the other hand is clearly less resolved and partly overlaps with intensity of the more weakly coupled protons (best resolved in the spectrum acquired at 3350.7 mT below 5 MHz). The H7a signals show a higher linewidth and

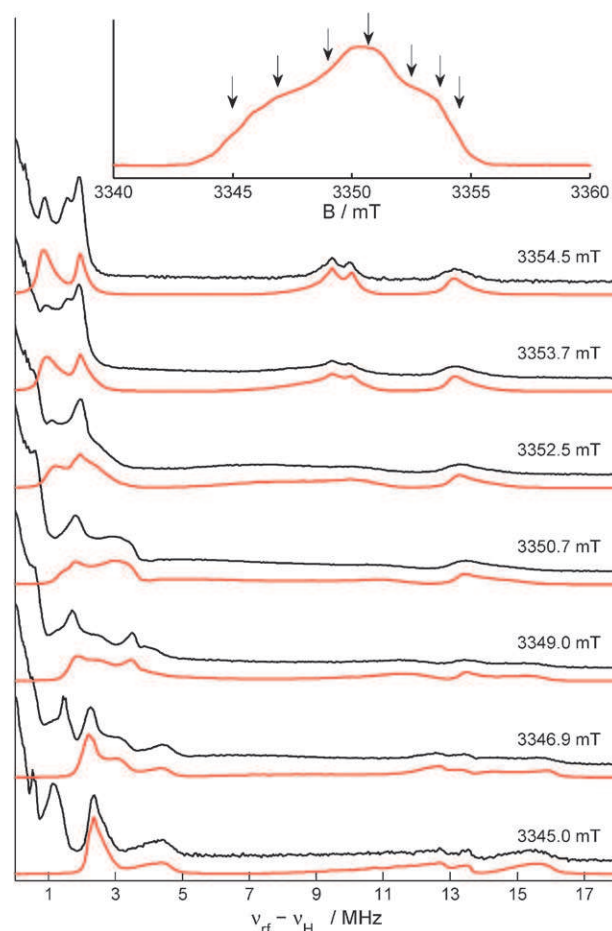


Fig. 4 Orientation-selective ENDOR at 94 GHz of Y_D^\bullet together with simulation (red). The field positions for the measurements are denoted. The spectra were taken at 40 K, shot repetition time 5 ms, $\pi_{mw} = 240$ ns, $\pi_{rf} = 23$ μ s. Inset on top: FSE of Y_D^\bullet at 94 GHz.

no discernible structure. Still, an estimation of the principal values and a first estimate of the tensor orientation can be obtained. There are several reports about the weaker couplings to the remaining ring protons H2 and H6 as well as the second β -proton H7b.^{26,37,38,40,41} These couplings are all smaller than 10 MHz. The corresponding signals are better resolved here than in earlier studies, owing to the orientation selection at 94 GHz. The assignment of the correct values for each proton needs further information, as there is no splitting resolved for the signals of H2 and H6 and, in addition to the protons under study here, some unassigned signals (*e.g.* from the hydrogen bond or protons from outside the Y_D^\bullet moiety) contribute to the spectral complexity. In essence, the initial analysis of the orientation-selective ENDOR spectra shown in Fig. 4 yielded

Table 1 Comparison of the g -tensor orientation within the crystal monomer to the molecular axes of TYR160 in the crystal structures of Loll *et al.*, 2005,²² (PDB entry 2AXT) and Guskov *et al.*, 2009,²³ (PDB entry 3BZ1). The molecular axes were determined by the vectors C4–C1 and C5–C3 (see Fig. 3). Shown are the directional cosines of the g -axes, or the molecular axes with respect to the crystal axes abc

	x	y	z	x_{3BZ1}	y_{3BZ1}	z_{3BZ1}	x_{2AXT}	y_{2AXT}	z_{2AXT}
a	0.163	0.253	0.954	0.164	0.212	0.964	0.270	0.103	0.958
b	−0.531	−0.793	0.301	−0.552	−0.794	0.267	−0.560	−0.794	0.242
c	0.832	−0.555	0.005	0.818	−0.570	−0.014	0.783	−0.599	−0.156

a more reliable set of starting parameters for the simulation of the single-crystal ENDOR spectra (see below). However, as our final hfc parameters were obtained by simultaneous simulations of the crystal ENDOR spectra and these orientation-selective frozen-solution spectra, we omit a detailed report on the intermediate results obtained from the initial analysis of the orientation-selective ENDOR on the frozen solution.

Single-crystal ^1H -ENDOR at 94 GHz. To obtain a full single-crystal ENDOR data set, we recorded a total of 58 spectra in the course of rotating the crystal with respect to the magnetic field. At each of the individual crystal orientations separated by 10° rotations ENDOR spectra were recorded at two to four field positions. In Fig. 5 and 6 we show a condensed version of our data presenting the sum of the spectra measured at the different field points for the individual crystal orientations. The field positions for the ENDOR spectra were chosen from a previously recorded and simulated set of EPR spectra along the same crystal rotation with the criterion being to obtain data for every crystal site at each crystal orientation. The full set of the 58 spectra is given in the ESI† along with a Figure detailing the field positions and

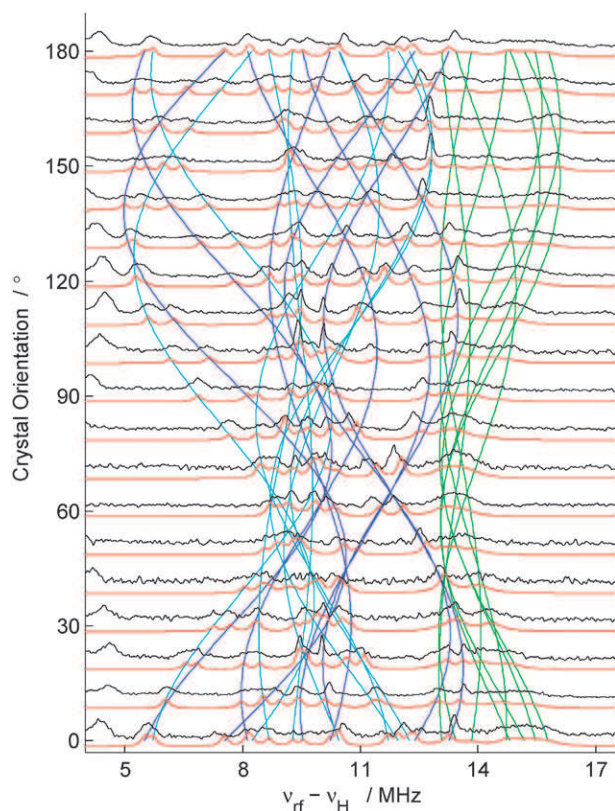


Fig. 5 Orientation-dependent pulse-ENDOR spectra of $\text{Y}_\text{D}^\bullet$ in single crystals of *Th. elongatus*. At each orientation Davies-ENDOR spectra are recorded at field positions corresponding to the particular crystal sites or their overlap positions in the EPR (see Fig. 2 and the illustrated course of the effective g -values). The spectra simulation is shown in red, the orientation dependence of the effective hyperfine values for H7a in green, H5 in dark blue, H3 in light blue. The spectra were taken at 40 K with a shot repetition time of 8 ms, $\pi_{\text{mw}} = 128$ ns, $\pi_{\text{rf}} = 16$ μs .

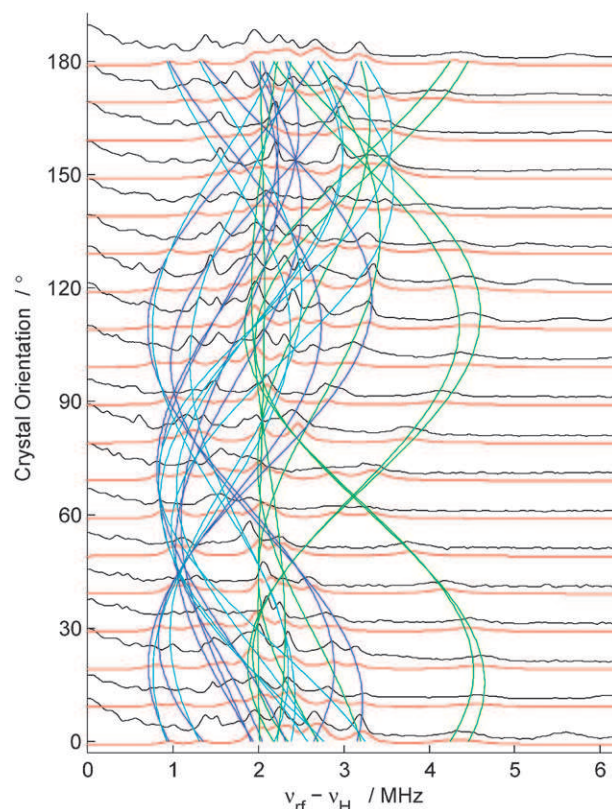


Fig. 6 Orientation-dependent pulse-ENDOR spectra of $\text{Y}_\text{D}^\bullet$ in single crystals of *Th. elongatus*, inner part. At each orientation Davies-ENDOR spectra are recorded at field positions corresponding to the particular crystal sites or their overlap positions in the EPR (see Fig. 2 and the illustrated course of the effective g -values). The spectra simulation is shown in red, the orientation dependence of the effective hyperfine values for H7b in green, H6 in dark blue, H2 in light blue.

crystal orientations at which they were recorded. As for the orientation-selective frozen-solution spectra only symmetrised half-spectra normalised to the free proton Larmor frequency are given. A clear site resolution of the individual $\text{Y}_\text{D}^\bullet$ is difficult to achieve even at W-band due to the rather large hfc compared to the g -factor resolution. This fact complicates the analysis of the single-crystal ENDOR data. However, our original data set given in the ESI† contains additional information about partial site resolution which is completely lost in the condensed version displayed in Fig. 5 and 6. Analysis of subsets of sites by simulation yields additional constraints which will not be discussed here for brevity.

Inspection of our simulated spectra shows they can be separated in two independent frequency ranges from 0 to about 5 MHz and from 5 to 17 MHz without indications of lines crossing the 5 MHz boundary. For clarity, we therefore present these two ranges in separate Figures. Fig. 5 presents the frequency region above 4.0 MHz and Fig. 6 shows the lower frequency range of the spectra below 6.2 MHz. The higher frequency range can immediately be attributed to the large H3, H5, and H7a couplings (in Fig. 5 coloured as light blue, dark blue and green, respectively). The lower frequency range carries the three couplings due to H2 (light blue in

Fig. 6), H6 (dark blue), and H7b (green) as well as weakly coupled nuclei from outside the Y_D^\bullet moiety (unassigned here), e.g. the H-bond to His189. According to earlier studies and corroborated by our frozen-solution ENDOR spectra, the frequency range beyond 14 MHz contains exclusively contributions from the H7a proton.

An interesting feature of our ENDOR spectra are the narrow, partially well-resolved lines in the frequency range from 5 to 14 MHz in Fig. 5, while the resonances at higher frequencies, attributed to H7a are broad and unresolved even in the single-crystal spectra. This very likely reflects a larger heterogeneity of the H7a β -proton couplings compared to the H3/H5 α -protons. A similar feature is visible in Fig. 6, where well-resolved lines arise in the 1 to 3 MHz range while only broad features are visible in the 3.5 to 5 MHz range (H7b).

Combined with the data gathered from orientation-selective frozen-solution ENDOR we arrived at hyperfine couplings for the protons H3, H5, and H7a as presented in Tables 2 and 3. Only minor refinements to their principal values derived from the frozen-solution spectra had to be made, though the single-crystal ENDOR spectra yielded exact values of A_y . As Fig. 5 shows, our simulation was successful in reproducing all discernible features of these protons, in particular their orientation dependence due to the rotation of the crystal. The differences between experiment and simulation in the position of some of the signals, up to about 200 kHz, appear reasonable due to the large number of simulation parameters involved, including the manually adjusted crystal rotation. Between 60° and 70° , the expected degeneracy of effective hyperfine couplings as seen in the single-crystal EPR is reflected in both, measurement and simulation. The broad signals of H7a appear unresolved in Fig. 5, but the course of the signals is reflected well in the simulations. The original orientation-selective data provide the separation of single signals that is lost in the sum (compare e.g. the different shape and position of the signals above 12.5 MHz in the spectra for the initial 0° crystal orientation in the ESI†). This enables us to report not only all the principal values but also the orientation of the H7a coupling.

In the central region of the ENDOR spectra, see Fig. 6, the spectral complexity is still high as the protons H2, H6, and H7b share comparable principal values and therefore overlap to a much higher degree in the region around 2 MHz. The large signals up to 5 MHz could be assigned to proton H7b and share the width shown by H7a. Along with the principal values, the orientation of the coupling could be assigned and is given in Table 3. The ambiguity concerning the principal

Table 3 Comparison of the hyperfine coupling principal values for the β -protons H7a and H7b. The orientations found in this work for the orientation of the couplings were (in Euler angles representing subsequent z , x' , and z'' rotations) (37, 12, -64) for the H7a hfc and (15, -24 , 8) for the H7b hfc, with an estimated experimental error of $\pm 5^\circ$ for the effective orientations. The experimental error of the principal values is assumed as ± 0.2 MHz

A_x^{H7a}	A_y^{H7a}	A_z^{H7a}	Ref.	A_x^{H7b}	A_y^{H7b}	A_z^{H7b}
32.2	26.8	26.0	This work	9.3	3.4	4.0
32.8	27.2	27.2	25			
31	28	27	42	9	7	3
30.5	27.0	27.0	36			
30.5	27.0	27.0	37	9.2	3.7	3.7
29.3	20.2	20.2	41	14.3	5.2	5.2
31.5	27.2	27.2	26	9.75	4.6	4.6
31.4	27.2	27.2	40	5.9	5.2	4.9

values of H2 and H6 in Fig. 4 could be resolved to obtain a full hfc tensor for both protons (see Table 4). Judging the simulations against the experimental spectra for this spectral region proved to be difficult, since not only the particular resonances overlap to a larger extent but also more weakly coupled and here unaccounted protons contribute to the spectra up to approximately 2 MHz. Resolving the hyperfine coupling of these protons, in particular that of the hydrogen bridge, is not within reach of the methods presented here and takes a different experimental approach.

Discussion of high-field ^1H -ENDOR on Y_D^\bullet . For comparing the hyperfine couplings found here to those previously reported by other authors (see Tables 2–4), it should be kept in mind that only in Hofbauer *et al.*²⁵ PSII from *Th. elongatus* was used. The differences to values reported by other authors could stem from differences in PSII preparations from different organisms. On the other hand, the remarkable agreement with the principal values reported in Rigby *et al.*²⁶ indicate a strong similarity of the electronic structure of Y_D^\bullet in PSII from *Th. elongatus* and spinach, which was also used in other studies.^{36,37,42} For the weakly coupled α -protons H2 and H6 only few reports can be found in literature as they are hard to resolve and to assign with low-frequency EPR techniques on frozen-solution samples, in particular the very small A_z component. While showing good agreement with those principal values reported by Rigby *et al.*,²⁶ we report complete sets of principal values along with their orientation with respect to the molecular frame for all six protons. For simulation purposes most other authors assumed the couplings of the β -protons H7a and H7b to be parallel to g_x , i.e. an orientation of (0,0,0). Some other studies^{26,37,36} stated the dihedral angle,

Table 2 Comparison of the hyperfine coupling principal values and orientations for the α -protons H3 and H5 of Y_D^\bullet in PSII. Formerly, it was not possible to assign values and orientations to each proton. Here, the values reported are ordered to correspond with our assignment of H3 and H5. We assume an experimental error of 0.1 MHz for the principal values and 1° for the angles

A_x^{H3}	A_x^{H5}	A_y^{H3}	A_y^{H5}	A_z^{H3}	A_z^{H5}	A_x^{H3}	A_x^{H5}	Ref.
-25.7	-27.3	-7.6	-8.4	-19.0	-20.2	-23.8	21.3	This work
$-25.5/-26.8$		≈ -8		$-19.0/-20.1$		± 20		25
24.0		3		19		± 26		42
23.0		14.8		18.8/20.3		± 30		36
23.0		12.3		18.8/20.3				37
-25.4		-7.2		19.5				41
$-25.6/-27.5$		-8.0		$-19.1/-20.5$		± 22		26

Table 4 Comparison of the hyperfine coupling principal values and orientations for the α -protons H2 and H6. We assume an experimental error of 0.2 MHz for the principal values and 2° for the angles

$A_x^{\text{H}2}$	$A_x^{\text{H}6}$	$A_y^{\text{H}2}$	$A_y^{\text{H}6}$	$A_z^{\text{H}2}$	$A_z^{\text{H}6}$	$A_L^{\text{H}2}$	$A_L^{\text{H}6}$	Ref.
4.7	4.5	7.4	7.1	1.5	1.4	22	−24	This work
3.7		7.0			3.7			37
4.8/4.4		7.4/7.15				∓ 10		26

obtained from the Heller–McConnell relation, which is not identical to the orientation of the actual hyperfine coupling. Differences for the H7 protons may also be caused by the inherent difficulties to obtain exact principal values from the broad unresolved signals assigned to them (and partly obscured by overlapping signals from α -protons in low-field studies) without information about the coupling orientation. This might explain the tendency of many of the reported values for H7a to overestimate the perpendicular components and underestimate the parallel one.

The combination of knowledge about the molecular orientation of the Y_D side chains in the PSII single crystal from X-ray crystallography, the assignment of the two large α -proton hfc in a tyrosine radical to the H3/H5 positions, the two small α -proton hfc to the H2/H6 positions, and of the principal axes of an α -proton hfc tensor to molecular axes together with the orientation-resolved hfc data from the single-crystal ENDOR experiments allow an unambiguous differentiation of the H3/H5 and H2/H6 hfc (see Fig. 1). The slight, but distinct differences in the hfc of the protons H3/H5 and H2/H6 reflect the asymmetry of the spin-density distribution in the molecule induced by the protein environment. This environment-induced asymmetry seems to be reflected by the orientation of the hyperfine tensors of the ring protons, too (see the differences in the Euler angles for the α -protons in Table 2 and 4). Attempts to shed light on the cause of this asymmetry by using density functional theory have been, so far, inconclusive. On one hand, Himo *et al.*⁴³ reported symmetry breaking mainly due to the hydrogen bonding of Y_D . On the other hand, Un⁴⁴ reported asymmetries in phenoxyl radicals as independent of hydrogen bonding and readily explainable by the position of an ethyl group acting as a substitute for the protein backbone. To disentangle the contributions of both effects, careful quantum chemical calculations including an adequate representation of the protein environment will be necessary. The results presented here, in particular the direction of the spin density asymmetry with more unpaired spin on C5 than C3 and on C2 than on C6, provide a benchmark for such calculations.

Recent reports about the strength of the hfc of the β -protons used the Heller–McConnell relation for the dependence of the isotropic hyperfine coupling to the dihedral angle of the proton to the π -orbital of the neighboring carbon C4, taking into account an empiric constant,^{26,37} or by spectra simulation of specific ^2H -labeled preparations.⁴⁵ Here, we have determined the orientation of the actual hyperfine coupling tensors. For the protons bound to C7 no simple relation to the molecular tetrahedral geometry is found. Comparison of the isotropic parts of both tensors (28.3 MHz for H7a, 5.6 MHz for H7b) with the Heller–McConnell relation yields results shown in Fig. 1. The Newman projection of the C7 carbon

onto the ring plane of Y_D shows the orientation of the two β -protons and the backbone carbon with respect to the ring. Because both β -hfc were determined the dihedral angles can be given directly from the measurements and don't rely on an empiric parameter. The resulting orientation is in very good agreement with the currently best-resolved crystal structure 3BZ1²³ with H7a showing a dihedral angle of 47° , H7b one of 73° , thus forming an angle of 119° , resp. 121° to the remaining C–C bond given by the structure.

In this part of the study we could therefore show how high-resolution ^1H -ENDOR spectroscopy enabled the complete mapping of the electronic structure of Y_D^\bullet in *Th. elongatus* to the ring protons and the β -protons of the side chain.

Q-Band EPR and ^{55}Mn -ENDOR on the S_2 -state MLS

Single-crystal ^{55}Mn -ENDOR results. High-field/high-frequency EPR and ENDOR have proven to be powerful tools to elucidate the orientation and assignment of the different ^1H -couplings of Y_D^\bullet and one would hope to profit from similar advantages by applying the same techniques to the S_2 -state MLS in PSII single crystals as successfully demonstrated in the case of the Mn-binding protein concanavalin A.⁴⁶ However, while EPR and ENDOR spectra of Mn^{2+} in concanavalin A consist of only narrow lines, the S_2 -state EPR MLS and the corresponding ENDOR spectra are extremely broad. The ENDOR spectra cover in X- and Q-band roughly the frequency range between 70 MHz and 180 MHz. This would result at W-band in an overlap of ^{55}Mn - and ^1H -ENDOR lines as the free proton Larmor frequency at W-band is in the range of 145 MHz. Furthermore, the increase of the ^{55}Mn Larmor frequency would shift the expected resonances for the largest coupling in WOC S_2 -state very close to or beyond the 200 MHz limitation of the Bruker DICE ENDOR accessory. Therefore, we employed EPR and ^{55}Mn -ENDOR spectroscopy at Q-band.

A prerequisite for the analysis of single-crystal ENDOR spectra is the knowledge of the crystal orientation within the laboratory frame. This was achieved again by analysis of single-crystal EPR spectra from Y_D^\bullet of the same sample used later for ENDOR. The analysis shows a rotation axis close to the crystallographic b -axis (for details see ESI†). Besides the Y_D^\bullet EPR spectra, orientation-dependent Q-band EPR spectra of the S_2 -state MLS were obtained and are shown in Fig. 7 together with a frozen-solution spectrum (shown in blue at the top).

The typical S_2 -state MLS with its multitude of resolved lines at about 9 mT separation in X-band spectra appears as a Gaussian-shaped unresolved line extending over 200 mT in Q-band FSE spectra. Some weak indications of the multiline structure can only be observed in the region between 1140 mT and 1180 mT. The region between 1180 mT and 1290 mT is

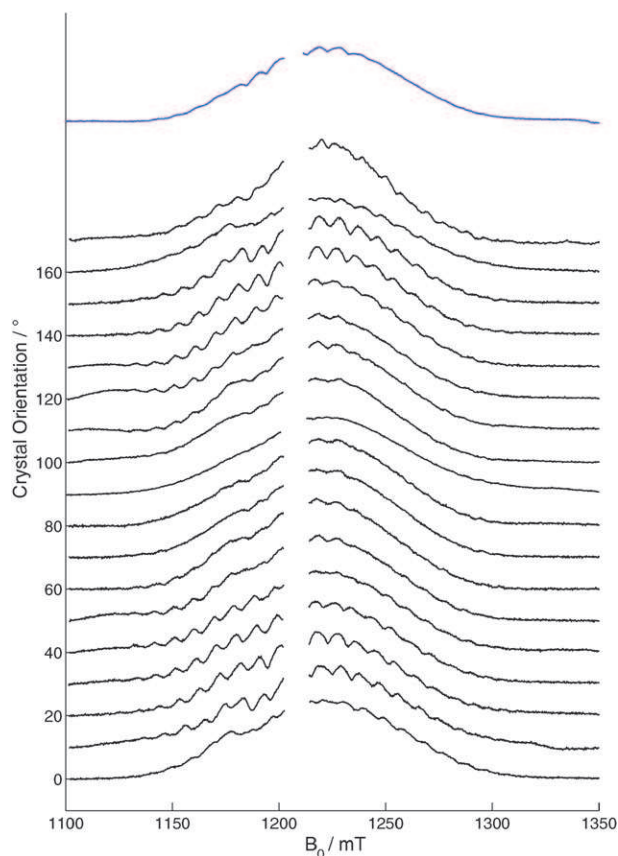


Fig. 7 Orientation-dependent EPR at 34 GHz of the S_2 -state MLS of single-crystal PSII prepared from *Th. elongatus*. On top in blue a FSE of the S_2 -state MLS of frozen-solution is shown. The Y_D signal is omitted for clarity. The rotation axis coincides approximately with the crystallographic b -axis. All spectra were taken at $T = 5$ K; the π -pulse had a length of 64 ns.

dominated by six troughs perturbing the MLS lineshape. They belong to traces of free Mn^{2+} present in the sample. These lines appear inverted compared to the MLS because the microwave pulses were optimised for the S_2 spin state $S_{eff} = 1/2$. As the flip angle depends on the spin state the $S = 5/2$, Mn^{2+} experiences a higher turning angle than a $S = 1/2$ spin resulting in an inverted echo signal causing the troughs in the MLS.

The S_2 -state MLS of the WOC with its four Mn ions consists of 1296 lines from each of the eight sites within the crystal unit cell. Thus, observed MLS FSE spectra shown in Fig. 7 are a superposition of many overlapping signals. Therefore, even measurements on single crystals don't improve the resolution of hyperfine-resolved lines in the EPR spectrum, as can be seen in Fig. 7. For some crystal orientations *e.g.* at 10° , 20° , 140° and 150° the superposition of g - and hyperfine structure results in up to 23 partially resolved lines spaced by roughly 9 mT. For other crystal orientations, *e.g.* 80° and 90° , this superposition leads to a destructive interference of g - and hyperfine structure resulting in a broad, almost featureless line. The same effect was already observed in W-band EPR on single crystals¹² and frozen solution.¹³

Due to the large ^{55}Mn hyperfine couplings no significant site selection effects are expected for ENDOR spectra recorded

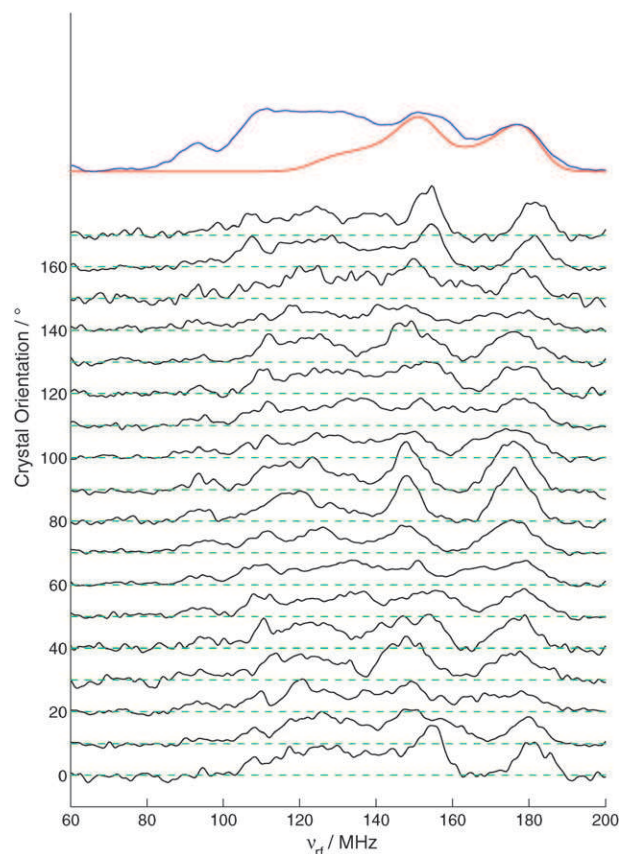


Fig. 8 Orientation-dependent ^{55}Mn -ENDOR spectra of the S_2 -state of single-crystal PSII. On top in blue a frozen-solution ^{55}Mn -ENDOR spectrum is shown together with a simulation of the ENDOR lines of the largest ^{55}Mn hyperfine tensor $A = (334, 334, 275)$ MHz in red. Crystal spectra were taken every 10° as denoted on the left, with the rotation axis approximately along the crystallographic b -axis. A baseline for each crystal spectrum is shown in green to guide the eye. All spectra were taken at $T = 5$ K with a microwave π -pulse of 64 ns and a RF-pulse of 4 μs at the field position 1230 mT.

within the central part of the MLS. Therefore, we decided to acquire ENDOR spectra for all crystal orientations and for a frozen-solution sample at one specific field position of 1230 mT on the maximum intensity of the MLS. The set of orientation-dependent ^{55}Mn -ENDOR single-crystal spectra together with a frozen-solution spectrum is shown in Fig. 8. The frozen-solution ^{55}Mn -ENDOR signal covers the spectral range from 80 MHz up to 200 MHz. Four broad but distinct lines at 95, 110, 153 and 178 MHz are superimposed upon broader and less resolved features. Between 110 and 140 MHz an almost featureless intensity is seen, flanked by the more pronounced lines at 110 and 153 MHz.

The ^{55}Mn -ENDOR frozen-solution spectrum of the S_2 -state MLS at 34 GHz prepared from MeOH-treated spinach PSII shown by Kulik *et al.*²⁹ has a similar overall spectral shape, covering the region between 70 MHz and 175 MHz. There, four resolved lines are found at about 80 MHz, 110 MHz, 130 MHz, and 170 MHz. The 153 MHz and 178 MHz peaks of the spectra of MeOH-untreated PSII samples prepared from *Th. elongatus* seem to correspond to a shoulder at about 140 MHz and the 170 MHz peak in the samples from

MeOH-treated spinach PSII, respectively. Both features are shifted to higher frequencies in our MeOH-untreated *Th. elongatus* samples as was similarly found for MeOH-untreated spinach.⁴⁷ A set of four axial hyperfine couplings, each contributing two tensorial lineshapes, one for the high- and the low-frequency resonance, respectively, split by approximately twice the nuclear Zeeman frequency was used to simulate the ⁵⁵Mn-ENDOR spectrum of the S₂-state MLS in spinach.⁴⁷ The simulation shows a strong overlap of resonances from two ⁵⁵Mn hyperfine tensors in the range from 80 to 100 MHz and from three ⁵⁵Mn hyperfine tensors in the range from 100 to 130 MHz. Between 130 and 150 MHz again hyperfine tensors originating from at least two ⁵⁵Mn nuclei contribute to the ENDOR signal. Beyond 150 MHz only the high-frequency line of the largest ⁵⁵Mn coupling is responsible for the ENDOR intensity.

To simulate this high-frequency region of our *Th. elongatus* frozen-solution spectrum, the largest hfc tensor $A = (310, 310, 275)$ MHz given by Kulik *et al.*⁴⁷ for MeOH-treated spinach PSII had to be adapted due to the shift of the ENDOR peaks to higher frequencies. The calculated line shapes for the two ENDOR transitions split by approximately twice the ⁵⁵Mn nuclear Larmor frequency (26 MHz at 1230 mT) of an axial hfc tensor $A = (334, 334, 275)$ MHz with a 13 MHz larger isotropic value stemming from an increased perpendicular component and a line width of 10 MHz reproduce well the two prominent high-frequency peaks of the experimental spectrum (see Fig. 8, top, red line).

Our single-crystal S₂-state ⁵⁵Mn-ENDOR spectra (Fig. 8) are quite similar to the frozen-solution spectrum and show much less gain in resolution compared to the situation for the ¹H-ENDOR on Y_D. Intensity in the low-frequency range below 100 MHz is clearly visible only for a few orientations (20°, 70°–100°, 140°). The limited signal-to-noise ratio (*S/N*) of the single-crystal spectra obscures the contributions in this frequency range. A broad unstructured ENDOR intensity is seen in the frequency range between 110 to 150 MHz as in the frozen solution. Also, the prominent features at about 150 and 180 MHz are well visible in all single-crystal spectra, with a small but discernible frequency variation between 150 to 153 MHz, and 178 to 181 MHz, respectively. These two features can again be assigned to the Mn ion with the largest hyperfine coupling in the WOC S₂-state as their orientation dependence is the same and their frequency difference fits to twice the Larmor frequency of ⁵⁵Mn at Q-band. Also the linewidth of these features is orientation dependent. From the stack plot presentation of the ⁵⁵Mn-ENDOR single-crystal spectra in Fig. 8 little orientational dependence of the spectral lines can be deduced.

The visibility of orientation-dependent features is improved in a two-dimensional contour representation as shown in Fig. 9. Besides the strong bands for the weakly orientation-dependent features around 150 and 180 MHz additional orientation-dependent intensity bands can now be identified. They connect the weakly orientation-dependent features and run from about 150 MHz up to about 180 MHz in the angular ranges 0°–30° and 40°–80°, respectively. Bands running in the opposite frequency direction down from about 180 MHz to about 150 MHz arise in the angular ranges of 90°–120° and

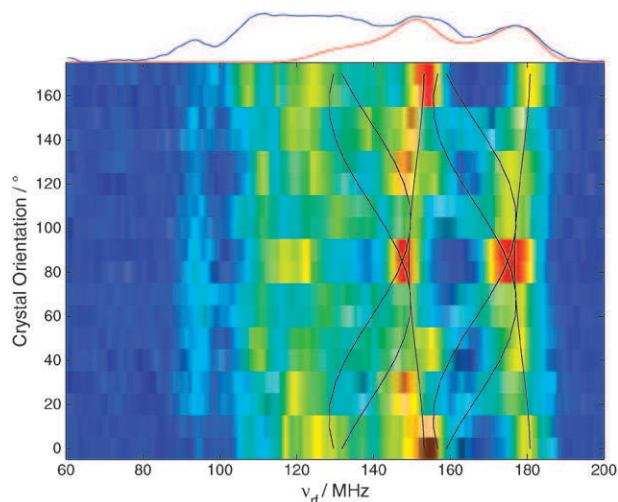


Fig. 9 Two-dimensional contour plot of the orientation-dependent ⁵⁵Mn-ENDOR single-crystal spectra of the S₂-state. Experimental parameters as in Fig. 8. Shown in black are the resonance positions of the largest ⁵⁵Mn hyperfine coupling $A = (334, 326, 275)$ MHz for all crystal sites. At the top a frozen-solution spectrum is shown in blue together with a simulation of the largest hfc in red.

130°–170°, respectively. Here, we concentrate our analysis of the ⁵⁵Mn-ENDOR single-crystal spectra to a discussion of the largest Mn hfc as above for the frozen-solution spectrum. The high-frequency ENDOR line for this coupling occurs in the region beyond 150 MHz and is well separated from the other seven ENDOR lines. A discussion of all four hyperfine couplings as well as their orientations would require an improved *S/N* in the spectra which can hardly be obtained.

Discussion of the single-crystal ⁵⁵Mn-ENDOR. The prominent weakly orientation-dependent features at about 150 and 180 MHz in the single crystal spectra occur at positions corresponding to the peaks at 153 and 178 MHz in the frozen-solution *Th. elongatus* sample. There the peaks arise from the Larmor-split perpendicular component of the axial hfc tensor for the largest ⁵⁵Mn coupling. The weak dependence of lines in this frequency range upon rotation of the single crystal can immediately be explained by an orientation of the unique axis of the axial hfc tensor for one or more sites in the crystal virtually parallel to the experimental rotation axis. In this case the magnetic field stays for all crystal orientations within or close to the perpendicular plane of the hfc tensor and thus gives at any crystal orientation rise to two features in the frequency ranges at 150 and 180 MHz, respectively. Bands connecting the 150 and 180 MHz ranges on the other hand can be explained by the 35 MHz anisotropy of the largest S₂-state Mn hfc in conjunction with the 7 MHz line width as used by Kulik *et al.*⁴⁷ for frozen solution of MeOH-treated spinach PSII. There, the axial line shapes for the high- and the low-frequency Larmor-split lines arising from the largest Mn hfc overlap in the 150 MHz range (see the top part of Fig. 3 in ref. 47). The observation of the full anisotropy of the hfc in a single crystal experiment requires an orientation of the unique axis of the largest hfc tensor virtually perpendicular to the crystal rotation axis for some sites in the unit cell. In this case

the magnetic field is aligned parallel to the unique axis for one particular crystal orientation (within an 180° variation) and is perpendicular to the magnetic field upon $\pm 90^\circ$ rotations. The full anisotropy of the tensor is covered for the orientations between these extrema. These two orthogonal alignments of the unique hfc tensor axis for different sites with respect to the crystal rotation axis can not be due to the $P2_12_12_1$ space group, as it connects the different sites in the unit cell by 180° rotations. However, PSII crystallises as a dimer connected by a non-crystallographic C_2 axis. This dimer symmetry axis does not coincide with any of the crystallographic axes and its bearing in the unit cell allows that both orientation requirements for the hyperfine tensor described above can in principle be met at the same time.

As for a part of the inequivalent sites in the unit cell, the orientation of the unique axis of the hyperfine tensor has to be parallel to the crystal rotation axis, this requires in our case (rotation roughly about the crystallographic b -axis) an almost parallel alignment of this axis with respect to the crystallographic b -axis. If this particular alignment of the unique hfc tensor axis for the Mn ion with the largest hfc occurs for one monomer at a specific site in the unit cell, this immediately also holds for all three other sites related by the $P2_12_12_1$ space group. This leads to the strong and only weakly orientation-dependent features around 150 and 180 MHz as they are due to four WOC sites in the unit cell. Interestingly, application of the non-crystallographic C_2 rotation relating the two PSII monomers within the dimer to this unique hfc axis results in an orientation of the image of this axis in the second monomer roughly perpendicular to the crystallographic b -axis (tilted approximately 22° out of the crystallographic ac -plane) and, thus also roughly perpendicular to the rotation axis in our experiment. Application of the symmetry elements of the $P2_12_12_1$ space group then results in two pairs of magnetically inequivalent sites with a unique hfc axis perpendicular to the rotation axis. These give rise to the two intensity bands running parallel from 150 MHz to 180 MHz and back (Fig. 9). The black lines in Fig. 9 represent calculations of the resonance positions for the largest ^{55}Mn hfc under the orientational assumptions given above. The angular splitting between the two parallel bands of about 40° is an immediate consequence of the discussed geometry and the crystal symmetry and is not a freely adjustable parameter of the simulations. The axial hfc tensor ($A = (334, 334, 275)$ MHz) used for the simulation of our frozen-solution spectra had to be slightly modified lifting the axial symmetry and allowing a slight rhombicity ($A = (334, 326, 275)$ MHz) in order to account for the observable orientation dependence of the lines at about 150 and 180 MHz.

Knowledge that the unique axis of the almost axial hfc tensor for the Mn ion with the largest hfc in the S_2 -state has to be roughly parallel to the crystallographic b -axis in one of the two PSII monomers alone is insufficient for an identification of a particular ion or its ligands in the crystallographic model of PSII. A prerequisite for this task is the additional knowledge about the connection between structural motifs and the unique hfc axis for the largest ^{55}Mn hfc. Previous studies²⁸ proposing the oxidation states in the S_2 -state of the WOC to be $\text{Mn}_3(\text{IV})\text{Mn}(\text{III})$, assigned the largest ^{55}Mn hfc to the Mn ion

in the oxidation state (III). The best studied model complexes, where a connection between structural motifs and the orientation of the $\text{Mn}(\text{III})$ hfc was drawn, are di- μ -oxo- μ -carboxylato bridged $\text{Mn}(\text{III})\text{Mn}(\text{IV})$ dimers. There, the unique axis of the large $\text{Mn}(\text{III})$ hfc was found to be perpendicular to the plane spanned by the $\text{Mn}-\text{O}_2-\text{Mn}$ core,^{48,49} i.e. nearly parallel to the terminal C–C bond in the carboxylate bridge.

Although due to radiation damage no precise positions of the Mn ions can be derived from the X-ray crystallography of PSII at present, the positioning of the amino acid side chains seems to be quite accurate as seen for the Y_D discussed in the first part of this work. Therefore, we used the crystal structure²³ to relate the orientation information from our ^{55}Mn -ENDOR analysis to the geometric structure of the ligand surrounding of the WOC.

For this task we assume that the unique hfc axis for the $\text{Mn}(\text{III})$ ion in the WOC is determined by the direction of the carboxylato-bridge as in dinuclear $\text{Mn}(\text{III})\text{Mn}(\text{IV})$ complexes. Fig. 10 shows the WOC within its protein environment, in particular the assigned bridging amino acids for both monomers (PDB entries 3BZ1/3BZ2). The crystallographic a -, b -, and c -axes are indicated in red, green and blue, respectively. As discussed above, the unique axis of the hfc is required to be oriented parallel to the crystallographic b -axis in one monomer. In the crystal structure only the terminal C–C-bond of the Asp342 carboxylato bridge in the 3BZ2 monomer is approximately parallel to the crystallographic b -axis (Fig. 10 right-hand side, the terminal C–C-bond is indicated by a black line), being tilted by 6° degrees away from the crystallographic b -axis. The terminal C–C-bond is at least tilted 30° away from the b -axis in either of the two monomers for all other amino acids. In the 3BZ1 monomer (Fig. 10 left-hand side) the terminal C–C-bond of Asp342 is tilted 25° out of the ac -plane. Both the 6° degree deviation of the C–C-bond of the Asp342 carboxylato bridge in the 3BZ2 monomer from the b -axis as the 25° out of the ac -plane alignment of this axis in the 3BZ1 monomer are in very good agreement with the orientations of the unique axis for the largest Mn hfc in the two PSII monomers in the WOC S_2 -state.

Asp342 ligates the Mn ions Mn1 and Mn2 in the notation of PDB entry 3BZ1/2. Kulik *et al.*⁴⁷ discussed various coupling schemes of the WOC in the S_2 -state. They suggested two probable assignments for the $\text{Mn}(\text{III})$ ion, giving rise to the largest Mn hfc in the S_2 -state, either to the Mn2 or the Mn4 position. Combining our result suggesting Mn1 or Mn2 with that of Kulik *et al.*,⁴⁷ we assign the Mn2 ligated by Asp342 as the $\text{Mn}(\text{III})$ ion in S_2 -state of the WOC. However, this assignment remains tentative, as there is neither conclusive agreement about the amino acids ligating the WOC nor about the coupling scheme between the Mn ions in the literature. Several models have been proposed for the amino acid ligands,^{4,50} not all of them taking Asp342 into account as a bridging ligand. Improved crystallographic models for the ligand environment of the WOC, more data relating hfc tensor axes to structural motifs in Mn complexes, as well as more elaborate coupling schemes for the Mn ions in the WOC are required to definitely assign the observed orientation of the unique $\text{Mn}(\text{III})$ hfc axis to the molecular structure of PSII.

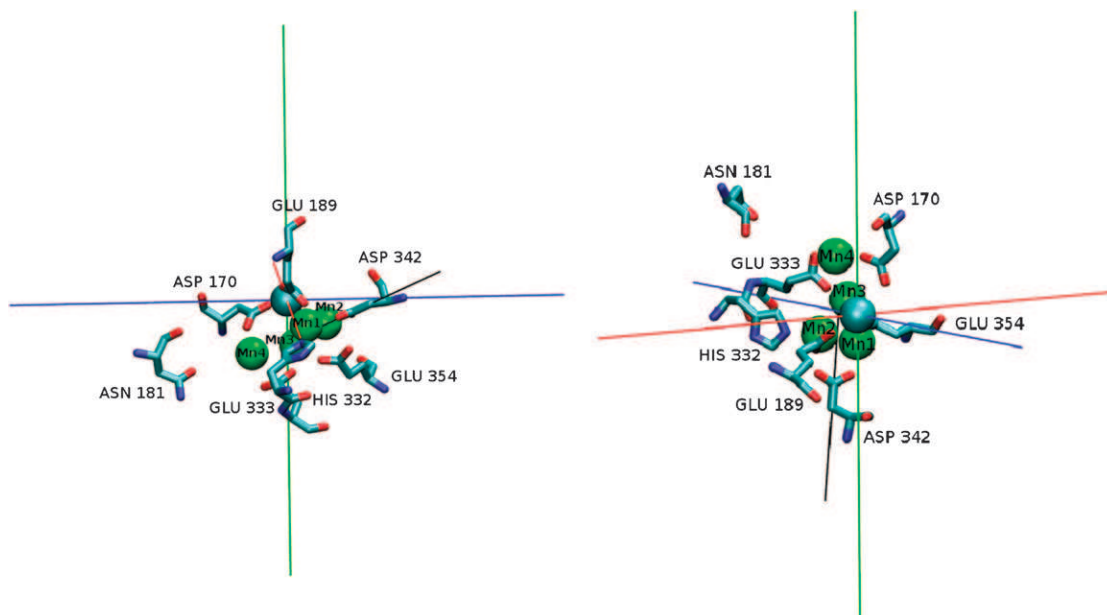


Fig. 10 Mn_4Ca cluster depicted from PDB entries 3BZ1 and 3BZ2 (left and right, respectively) for the two PSII monomers together with surrounding ligands. The crystallographic axes system is depicted as centered at the Ca ion with the a -axis in red, the b -axis in green and the c -axis in blue. The direction of the Asp342 carboxylate C–C axis is coloured in black.

Conclusions

In this paper, we have assigned complete hyperfine coupling tensors by W-band ^1H -ENDOR on PSII single crystals to all of the covalently bound protons of the amino acid side chain of $\text{Y}_\text{D}^\bullet$ in PSII. Thereby, a complete map of the electronic structure of this model amino acid radical has been deduced. The combination of structural information from crystallography with EPR and ENDOR results allowed an unambiguous assignment of the slightly different couplings for the H3/H5 and the H2/H6 protons which are equivalent in a phenoxyl radical but become magnetically inequivalent due to the amino acid backbone and asymmetries induced by the binding pocket, e.g. asymmetric hydrogen bonding or the side chain orientation. The spin density asymmetry in the $\text{Y}_\text{D}^\bullet$ ring presented here, reporting larger spin density on C2 and C5 than on the symmetry related positions C6 and C3, should stimulate quantum chemical calculations providing a conclusive picture of the protein surrounding effects leading to the specific electronic structure of the $\text{Y}_\text{D}^\bullet$ in PSII.

In the second part of this study, we presented the application of ^{55}Mn -ENDOR at Q-band frequencies to the S_2 -state of the WOC in PSII which consists of a complex multi-nuclear metal cluster. The presented first orientation-dependent ^{55}Mn -ENDOR spectra obtained from a PSII single crystal clearly corroborate the qualitative features of the hfc tensor for the $\text{Mn}(\text{III})$, i.e. the Mn ion with the largest hfc, in the WOC S_2 -state as deduced by Kulik *et al.*⁴⁷ from frozen-resolution spinach PSII. The virtual crystal orientation independence of lines arising for this coupling upon rotation about an axis very close to the crystallographic b -axis together with the unit cell symmetry and the dimeric nature of the crystallised PSII immediately yield a completely determined model for the orientation of the unique axis of the oblate hfc tensor

for this ion in both PSII monomers at the four dimer sites within the unit cell. Under the assumption of a specific relation between the ligand environment and the hfc tensor inspired by earlier results on di-nuclear Mn complexes we suggest Asp342 being a likely ligand to the $\text{Mn}(\text{III})$ ion in the S_2 -state. This is an important step towards the identification of the Mn ions changing their oxidation state in the course of the S-state cycle of photosynthetic water splitting. Knowledge about the redox-active Mn ions in the cluster is a prerequisite for a discussion of the water-splitting catalysis in terms of mechanistic reaction models.

Acknowledgements

We are grateful to a reviewer for valuable comments. This work was supported by Deutsche Forschungsgemeinschaft through Sfb-498 ‘‘Protein-Cofactor Interactions’’ TP C5 and C7.

References

- 1 *Photosystem I The Light-Driven Plastocyanin: Ferredoxin Oxidoreductase*, ed. J. H. Golbeck, Springer, 2006, vol. 24.
- 2 *Photosystem II The Light-Driven Water: Plastoquinone Oxidoreductase*, ed. T. J. Wydrzynski and K. Satoh, Springer, 2006, vol. 22.
- 3 J. P. McEvoy and G. W. Brudvig, *Chem. Rev.*, 2006, **106**, 4455–4483.
- 4 J. Barber, *Inorg. Chem.*, 2008, **47**, 1700–1710.
- 5 A. W. Rutherford, A. Boussac and P. Faller, *Biochim. Biophys. Acta, Bioenerg.*, 2004, **1655**, 222–230.
- 6 J. H. A. Nugent, R. J. Ball and M. C. W. Evans, *Biochim. Biophys. Acta, Bioenerg.*, 2004, **1655**, 217–221.
- 7 M. Sugiura, F. Rappaport, K. Brettel, T. Noguchi, A. W. Rutherford and A. Boussac, *Biochemistry*, 2004, **43**, 13549–13563.
- 8 W. Lubitz, F. Lendzian and R. Bittl, *Acc. Chem. Res.*, 2002, **35**, 313–320.

- 9 J. M. Peloquin and R. D. Britt, *Biochim. Biophys. Acta, Bioenerg.*, 2001, **1503**, 96–111.
- 10 B. Kok, B. Forbush and M. McGloin, *Photochem. Photobiol.*, 1970, **11**, 457–475.
- 11 D. H. Kim, R. D. Britt, M. P. Klein and K. Sauer, *Biochemistry*, 1992, **31**, 541–547.
- 12 H. Matsuoka, K. Furukawa, T. Kato, H. Mino, J. R. Shen and A. Kawamori, *J. Phys. Chem. B*, 2006, **110**, 13242–13247.
- 13 C. Teutloff, S. Kessen, J. Kern, A. Zouni and R. Bittl, *FEBS Lett.*, 2006, **580**, 3605–3609.
- 14 S. Turconi, D. J. MacLachlan, P. J. Bratt, J. H. A. Nugent and M. C. W. Evans, *Biochemistry*, 1997, **36**, 879–885.
- 15 G. J. Yeagle, M. L. Gilchrist, R. M. McCarrick and R. D. Britt, *Inorg. Chem.*, 2008, **47**, 1803–1814.
- 16 H. Yamada, H. Mino and S. Itoh, *Biochim. Biophys. Acta, Bioenerg.*, 2007, **1767**, 197–203.
- 17 G. C. Dismukes and Y. Siderer, *FEBS Lett.*, 1980, **121**, 78–80.
- 18 J. R. Shen and N. Kamiya, *Biochemistry*, 2000, **39**, 14739–14744.
- 19 A. Zouni, H. T. Witt, J. Kern, P. Fromme, N. Krauss, W. Saenger and P. Orth, *Nature*, 2001, **409**, 739–743.
- 20 N. Kamiya and J. R. Shen, *Proc. Natl. Acad. Sci. U. S. A.*, 2003, **100**, 98–103.
- 21 K. N. Ferreira, T. M. Iverson, K. Maghlaoui, J. Barber and S. Iwata, *Science*, 2004, **303**, 1831–1838.
- 22 B. Loll, J. Kern, W. Saenger, A. Zouni and J. Biesiadka, *Nature*, 2005, **438**, 1040–1044.
- 23 A. Guskov, J. Kern, A. Gabdulkhakov, M. Broser, A. Zouni and W. Saenger, *Nat. Struct. Mol. Biol.*, 2009, **16**(3), 334–342.
- 24 J. Yano, J. Kern, K. D. Irrgang, M. J. Latimer, U. Bergmann, P. Glatzel, Y. Pushkar, J. Biesiadka, B. Loll, K. Sauer, J. Messinger, A. Zouni and V. K. Yachandra, *Proc. Natl. Acad. Sci. U. S. A.*, 2005, **102**, 12047–12052.
- 25 W. Hofbauer, A. Zouni, R. Bittl, J. Kern, P. Orth, F. Lenzian, P. Fromme, H. T. Witt and W. Lubitz, *Proc. Natl. Acad. Sci. U. S. A.*, 2001, **98**, 6623–6628.
- 26 S. E. Rigby, J. H. Nugent and P. J. O'Malley, *Biochemistry*, 1994, **33**, 1734–1742.
- 27 D. W. Randall, B. E. Sturgeon, J. A. Ball, G. A. Lorigan, M. K. Chan, M. P. Klein, W. H. Armstrong and R. D. Britt, *J. Am. Chem. Soc.*, 1995, **117**, 11780–11789.
- 28 J. M. Peloquin, K. A. Campbell, D. W. Randall, M. A. Evanchik, V. L. Pecoraro, W. H. Armstrong and R. D. Britt, *J. Am. Chem. Soc.*, 2000, **122**, 10926–10942.
- 29 L. V. Kulik, B. Epel, W. Lubitz and J. Messinger, *J. Am. Chem. Soc.*, 2005, **127**, 2392–2393.
- 30 S. Pudollek, F. Lenzian and R. Bittl, *Biochem. Soc. Trans.*, 2008, **36**, 1001–1004.
- 31 J. Kern, B. Loll, C. Lüneberg, D. DiFiore, J. Biesiadka, K. D. Irrgang and A. Zouni, *Biochim. Biophys. Acta, Bioenerg.*, 2005, **1706**, 147–157.
- 32 S. Stoll and A. Schweiger, *J. Magn. Reson.*, 2006, **178**, 42–55.
- 33 B. E. Sturgeon, J. A. Ball, D. W. Randall and R. D. Britt, *J. Phys. Chem.*, 1994, **98**, 12871–12883.
- 34 M. Rohrer, F. MacMillan, T. Prisner, A. Gardiner, K. Möbius and W. Lubitz, *J. Phys. Chem. B*, 1998, **102**, 4648–4657.
- 35 M. Bennati, C. T. Farrar, J. A. Bryant, S. J. Inati, V. Weis, G. J. Gerfen, P. Riggs-Gelasco, J. Stubbe and R. G. Griffin, *J. Magn. Reson.*, 1999, **138**, 232–243.
- 36 C. T. Farrar, G. J. Gerfen, R. G. Griffin, D. A. Force and R. D. Britt, *J. Phys. Chem. B*, 1997, **101**, 6634–6641.
- 37 M. Gilchrist, J. Ball, D. Randall and R. Britt, *Proc. Natl. Acad. Sci. U. S. A.*, 1995, **92**, 9545–9549.
- 38 C. W. Hoganson and G. T. Babcock, *Biochemistry*, 1992, **31**, 11874–11880.
- 39 P. O'Malley and D. Ellson, *Biochim. Biophys. Acta, Bioenerg.*, 1997, **1320**, 65–72.
- 40 B. A. Barry and G. T. Babcock, *Chem. Scr.*, 1988, **28A**, 117.
- 41 K. Warncke, G. Babcock and J. McCracken, *J. Am. Chem. Soc.*, 1994, **116**, 7332–7340.
- 42 P. Dorlet, A. Rutherford and S. Un, *Biochemistry*, 2000, **39**, 7826–7834.
- 43 F. Himo, A. Gräslund and L. A. Eriksson, *Biophys. J.*, 1997, **72**, 1556–1567.
- 44 S. Un, *Magn. Reson. Chem.*, 2005, **43**, S229–S236.
- 45 Alia, B. Hulsebosch, H. van Gorkom, J. Raap, J. Lugtenburg, J. Matysik, H. de Groot and P. Gast, *Chem. Phys.*, 2003, **294**, 459–469.
- 46 K. V. Narasimhulu, R. Carmieli and D. Goldfarb, *J. Am. Chem. Soc.*, 2007, **129**, 5391–5402.
- 47 L. V. Kulik, B. Epel, W. Lubitz and J. Messinger, *J. Am. Chem. Soc.*, 2007, **129**, 13421–13435.
- 48 K. Schäfer, R. Bittl, W. Zweggart, F. Lenzian, G. Haselhorst, T. Weyhermüller, K. Wieghardt and W. Lubitz, *J. Am. Chem. Soc.*, 1998, **120**, 13104–13120.
- 49 K. Schäfer, R. Bittl, F. Lenzian, V. Barynin, T. Weyhermüller, K. Wieghardt and W. Lubitz, *J. Phys. Chem. B*, 2003, **107**, 1242–1250.
- 50 S. Zein, L. V. Kulik, J. Yano, J. Kern, Y. Pushkar, A. Zouni, V. K. Yachandra, W. Lubitz, F. Neese and J. Messinger, *Philos. Trans. R. Soc. London, Ser. B*, 2008, **363**, 1167–1177.